CCFE
CULHAM CENTRE FOR FUSION ENERGY

UK Atomic Energy Authority

UKAEA-CCFE-PR(20)14

Dylan Agius, Abdullah Al Mamun, Chris A Simpson, Christopher Truman, Yiqiang Wang, Mahmoud Mostafavi, David Knowles

Microstructure-informed, predictive crystal plasticity finite element model of fatigue-dwells

Microstructure-informed, predictive crystal plasticity finite element model of fatigue-dwells

Dylan Agius, Abdullah Al Mamun, Chris A Simpson, Christopher Truman, Yiqiang Wang, Mahmoud Mostafavi, David Knowles

This is a preprint of a paper submitted for publication in Computational Materials Science

Microstructure-informed, predictive crystal plasticity finite element model of fatigue-dwells

Dylan Agius[a], Abdullah Al Mamun[a], Chris A Simpson[a], Christopher Truman[a], Yiqiang Wang[b], Mahmoud Mostafavi[a] and David Knowles[a]

[a]Solid Mechanics Research Group, Department of Mechanical Engineering, University of Bristol, Bristol BS8 1TR, UK

[b]United Kingdom Atomic Energy Authority, Culham Science Centre, Abingdon OX14 3DB, UK

Abstract

Crystal plasticity finite element (CPFE) modelling is an effective tool from which detailed information on the meso-scale behaviour of crystalline metallic systems can be extracted and used, not only to enhance the understanding of material behaviour under different loading conditions, but also to improve the structural integrity assessment of engineering components. To be of full benefit however it must be demonstrated to not only predict the average global response of the material, but also the local behaviour, which controls damage. In this study, a slip system based constitutive model is developed to improve the simulation capability of time independent and time dependent plasticity. Comparison has been made between the macro-mechanical behaviour predicted by the model and previous experiments carried out at engineering length scale. Critically, the macro-mechanical behaviour predicted by the model has been examined against the behaviour of the materials at meso-scale crystalline level measured by previous diffraction experiments. The robustness of the model is demonstrated on both the macro- and meso-scale through the successful prediction of macro-scale behaviour and lattice strain evolution under a variety of loading conditions. The model not only effectively recognised the influence of prior deformation on subsequent loading, but also complemented neutron diffraction data to enrich the understanding of the influence of an important loading condition on the deformation of grains within the material.

Key words: Crystal plasticity, Creep, Stress relaxation, Stainless Steel

1. Introduction

Since complex thermomechanical loading is expected during operation of a power plant, it is vitally important to not only understand the influence of these complex load histories on the life of components, but also on the micro-mechanisms within their materials. Doing so provides an improved understanding of the deformation of material in the components, but critically a greater insight into the influence of the micromechanics, which dominate damage, such that life extension can be achieved with greater assurance. This also allows for the enhanced evaluation of more suitable materials for future design and construction of components.

Computational materials engineering using crystal plasticity finite element (CPFE) modelling can provide aspects of insight into the behaviour of the crystalline material when subject to complex load histories. The recognition of this approach to integrate CPFE into the design of materials has been gaining popularity through the emergence of integrated computational materials engineering (ICME) methodologies over the last few years. It has also been fuelled by the drive to integrate the processing-microstructure-property-relationships in the design process of materials. Recent examples of the success of ICME approaches include the work by Tin, Detrois, Rotella and Sangid [1] who used ICME to modify a Ni-based superalloy to improve its damage-tolerance. In addition, CPFE approaches have also been utilised to extract deeper insight into the local deformation of the material which is on occasion difficult to obtain experimentally, an approach utilised by Tasan, Hoefnagels, Diehl, Yan, Roters and Raabe [2] to compliment experimental data in the investigation of microstructural strain and stress partitioning in ferritic-martensitic dual phase steels. Furthermore, Sinha, Szpunar, Kiran Kumar and Gurao [3] used CPFE, in conjunction with electron backscatter diffraction data, to develop deeper understanding around the influence of twinning during tensile loading of 316L stainless steel.

There are a number of different phenomena which can affect the life of metallic components exposed to complex thermo-mechanical loading history. These include time-dependent permanent deformation such as strain accumulation and stress relaxation occurring during creep. Both strain accumulation and stress relaxation can occur during plant operation due to loading conditions which induce either load or displacement-controlled deformation or a combination of both. Therefore, it is important to develop an understanding of how these phenomena evolve to provide greater insight on their influence on the life of components within the plant. Such an approach was used by Song, Sun, Li, Xu, Rawlings, Liebscher, Clausen, Poplawsky, Leonard, Huang, Teng, Liu, Asta, Gao, Dunand, Ghosh, Chen, Fine and Liaw [4] in development of a ferritic alloy with improved creep resistance, achieved through the findings associated with the integration of advanced experimental tools (including transmission-electron microscopy, neutron diffraction, and atom-probe tomography) and CPFE. The creep resistance was enhanced through the inclusion of coherent hierarchical precipitates, the influence of which was quantified through the integration of these different tools, ultimately providing greater understanding of the interactions between the deformation of the matrix and the precipitates.

Further development in understanding has also extended to consideration of the influence of cyclic loading on creep deformation. Cyclic deformation can occur due to periodic shutdowns and scheduled maintenance [5]. The influence of the generated cyclic deformation on creep in austenitic stainless steels from a macro-scale deformation has been investigated experimentally, with the findings indicating that the evolution of creep strain and stress relaxation can be affected by prior cyclic loading [6-8]. Additionally, experimental investigation on the local level using neutron diffraction has also been conducted by [9-11] to provide greater insight into the contribution of intergranular stresses generated during cyclic loading on the creep deformation. These studies have highlighted the differences in grain-to-grain interactions occurring during plasticity and creep resulting in different levels of anisotropy. This additional experimental investigation is vital in generating a more detailed insight of the underlying micromechanics of deformation which contribute to the macro-scale deformation.

To complement the experimental investigation into creep and prior cyclic loading on creep, there has been a significant push towards using micromechanical models, which include self-consistent models (SCM) [12] and CPFE. SCM have been used to simulate the deformation of austenitic stainless steels subject to different loading conditions. Stress relaxation has been investigated using SCM [13], and modifications were made to the underlying constitutive equations to improve creep simulations by Hu and Cocks [14]. Additionally, the effect of thermal aging on creep deformation was investigated by Chen, Hu, Flewitt, Cocks, Ainsworth, Smith, Dean and Scenini [15] and Wang, Jeong, Clausen, Liu, McCabe, Barlat and Tomé [16] considered the effect of martensitic phase transformation. Further modifications were also introduced by Petkov, Hu and Cocks [5] to improve the SCM capabilities to simulate macroscopic stress relaxation, creep strain evolution, and the influence of prior cyclic loading on creep.

In addition to the investigation of austenitic stainless steels using SCM, CPFE has also grown in popularity to provide in depth knowledge of the structural integrity of the material. The focus of this understanding has included damage evolution and crack initiation [17-20], influence of grain morphology and orientation on local deformation [21, 22], lattice strain evolution [17, 23-27] and low-cycle fatigue [28]. CPFE has also been applied to investigate the evolution of creep strain. Petkov, Hu, Tarleton and Cocks [29] used a CPFE model to simulate the evolution of creep strain, which was then compared to the predictions made using a SCM modelling approach. Additionally, Erinosho, Venkata, Mostafavi, Knowles and Truman [30] investigated the influence of prior cyclic plastic loading on creep strain and introduced a modification to constitutive model controlling slip hardening to improve the deformation during the creep regime. Although CPFE modelling has been applied to understand the creep deformation under load-controlled dwells in austenitic stainless steels, limited work has been undertaken to understand how the predictive capabilities of these constitutive models translate to creep deformation during displacement-controlled (stress relaxation) dwells. This is a particularly important investigation to undertake in the development of a CPFE modelling capability to develop a robust modelling approach proficient in recognising the differences in lattice strain evolution during both constant load- and strain-controlled creep.

In this study, a crystal plasticity constitutive model for 316H stainless steel has been developed to predict the amount of expected stress relaxation during single and multiple load-displacement dwells using previous experimental data by [31-33] and Mamun, Simpson, Agius, Reinhard, Truman, Mostafavi and Knowles [9]. The modifications made to the underlying constitutive models (superposition of power laws, addition of type III residual stress, and the addition of recovery to the developed hardening) and the justification for the modifications are detailed based on microscopic behaviours of the material. A parameter calibration scheme is also detailed to ensure application of the constitutive models to other materials. Finally, the CPFE is used to provide deeper understanding on the influence of local grain environmental effects on the deformation of crystals by simulating the lattice strain evolution and comparing the results to an experimental investigation undertaken by Wang, Hossain, Kabra, Zhang, Smith and Truman [33].

2. Constitutive Model Development for Crystal Plasticity Modelling

In the following sections the crystal plasticity governing equations will be introduced to provide background on how crystal deformation is calculated. The constitutive relationships adopted will

then be given, followed by the modifications introduced to incorporate phenomenologically the microscopic behaviours (e.g. creep and the associated hardening and recovery phenomena) occurring in the material.

2.1 Kinematics

The following kinematic theory is based on the work described in [34-37], the history of which was reviewed in [38]. The summary presented is also based on the work by Huang [39].

The total crystal deformation ($\boldsymbol{F}$) can be described based on the contributions of both the plastic and elastic deformations, using the assumption that the deformation gradient obeys a multiplicative decomposition as given in the following equation,

$$\boldsymbol{F} = \boldsymbol{F}^e \boldsymbol{F}^p \tag{1}$$

where $\boldsymbol{F}^p$ is the plastic deformation associated with crystallographic slip, and $\boldsymbol{F}^e$ is the elastic deformation associated with rigid body rotation and elastic stretching of the crystal lattice.

The velocity gradient can be calculated using the following,

$$\boldsymbol{L} = \dot{\boldsymbol{F}}\boldsymbol{F}^{-1} = \boldsymbol{D} + \boldsymbol{\Omega} \tag{2}$$

where $\boldsymbol{D}$ is the stretch tensor and $\boldsymbol{\Omega}$ the spin tensor respectively. These two tensors representing stretch and spin can themselves be decomposed into lattice and plastic parts,

$$\boldsymbol{D} = \boldsymbol{D}^e + \boldsymbol{D}^p, \quad \boldsymbol{\Omega} = \boldsymbol{\Omega}^e + \boldsymbol{\Omega}^p \tag{3}$$

where $\boldsymbol{D}^p$ and $\boldsymbol{\Omega}^p$ are plastic stretch tensor and plastic spin tensor respectively. These plastic tensors result from crystallographic slip which can be captured by the following relations,

$$\boldsymbol{D}^e + \boldsymbol{\Omega}^e = \dot{\boldsymbol{F}}^e \boldsymbol{F}^{e-\mathbf{1}}, \quad \boldsymbol{D}^p + \boldsymbol{\Omega}^p = \sum_{\alpha=1}^{N_s} \dot{\gamma}^\alpha \boldsymbol{s}^{*\alpha} \otimes \boldsymbol{m}^{*\alpha} \tag{4}$$

where N_s is the number of slip systems, $\dot{\gamma}^\alpha$ is the slip rate on slip system α, $\boldsymbol{s}^{*\alpha}$ and $\boldsymbol{m}^{*\alpha}$ represents the vector along the slip direction and the vector representing the normal to the slip plane of system α in the deformed configuration respectively,

$$\boldsymbol{s}^{*\alpha} = \boldsymbol{F}^e \boldsymbol{s}^\alpha, \quad \boldsymbol{m}^{*\alpha} = \boldsymbol{m}^\alpha \boldsymbol{F}^{e-1} \tag{5}$$

where $\boldsymbol{s}^\alpha$ and $\boldsymbol{m}^\alpha$ are the unit vectors in the slip direction and normal to the slip plane in the reference configuration respectively.

2.2 Constitutive Models

Based on the kinematic formulations presented above it are the magnitudes of $\dot{\gamma}^\alpha$ on the active slip systems which are the primary focus of development for crystal plasticity models [40].

Slip can be modelled using a visco-plastic power-law relation following the work by [41, 42],

$$\dot{\gamma}^\alpha = \dot{\gamma}_0 \left(\frac{\tau^\alpha}{g^\alpha}\right)^n sgn(\tau^\alpha) \tag{6}$$

where $\dot{\gamma}_o$ is a reference strain rate, τ^α is the resolved shear stress on the slip system α, g^α is a measure of the material's resistance to slip on the slip system α (which relates to strain hardening and/or softening) and n is a strain rate sensitivity parameter. Altering the value of n can reflect the sensitivity of the strain rate.

Slip system hardening can evolve according to a phenomenological based formulation of accumulated shear flow, which is an average plastic shear strain representing the overall effect of dislocation movement [43]. The evolution adopted for this work is that proposed by McGinty and McDowell [44]. This version of hardening model is based on the assumption made by Taylor [34] where all activated slip systems result in equal hardening across all slip systems. Therefore, the applied slip hardening model can be described as slip system isotropic hardening. The slip hardening has the following evolution,

$$\dot{g^\alpha} = h_0 \sum_{\beta=1}^{N_s} \left\{ \left(1 + \frac{h_0 \gamma_{sum}}{\tau_0 m} \right)^{m-1} \left| \dot{\gamma}^\beta \right| \right\} \tag{7}$$

where h_0 is the initial hardening modulus, m is a fitting parameter used to alter the rate of saturation, and τ_0 the initial critical resolved shear stress. γ_{sum} is the total accumulated inelastic shear strain on all slip systems which evolves according to Eq 8,

$$\gamma_{sum} = \sum_{\beta=1}^{N_s} \int_0^t \left| \dot{\gamma}^\beta \right| dt \tag{8}$$

2.3 Constitutive Model Modifications

In the following sections, the modifications made to the basic constitutive equations proposed in the previous sections, explained from a microstructure influence, are outlined alongside a description of the meso-scale stress state which evolves in a polycrystalline metallic system under plastic deformation.

2.3.1 Type III Residual Stress (Intragranular)

One of the benefits of CPFE method is it incorporates intrinsically the capability to generate type II residual stress (intergranular) associated with grain to grain kinematic effects [45]. However, to further improve the CPFE model it was found necessary to also include local type III residual stresses (intragranular) into the constitutive model to recognise their influence on the deformation of the polycrystal as indicated by Hu, Chen, Smith, Flewitt and Cocks [46]. To incorporate the type III residual stresses, the slip rate constitutive relation given in Eq 6 was modified to give the following,

$$\dot{\gamma}^\alpha = \dot{\gamma}_0 \left(\frac{\left| \tau^\alpha - X^\alpha \right|}{g^\alpha} \right)^n sgn(\tau^\alpha - X^\alpha) \tag{9}$$

X^α in Eq 9 is the type III residual stress, which in this study evolves according to the Armstrong-Fredrick (AF) model [47] expressed as,

$$\dot{X}^{\alpha} = h\dot{\gamma}^{\alpha} - h_D X^{\alpha}|\dot{\gamma}^{\alpha}| \tag{10}$$

where h is the direct hardening coefficient and h_D controls the dynamic recovery associated with the annihilation process between mobile and immobile dislocation links of opposite signs [12]; the ratio of the values (h/h_D) controls the saturation level of X^{α} in each slip system [48]. The inclusion of type III residual stress through an AF formulation is a phenomenological approach proposed by several researchers [49-51] but has since gathered even greater popularity.

The current formulation assumes that the evolution of the type III residual stress is dependent on slip within its own slip system, thus its evolution does not depend on slip on other systems, which is unlike the formulation proposed by Xu and Jiang [40]. The reasoning was to ensure simplicity of application as the current formulation requires only two calibrating parameters. Therefore, a simpler formulation of X^{α} was derived to provide a baseline for simulation and experimental comparisons.

2.3.2 Decomposing the Flow Rule into Components of Plasticity and Creep

Creep can be caused by diffusion-controlled climb, which can be thought of as a two-step process as discussed by Duffin and Nichols [52]. A slip plane containing dislocations restricted by obstacles can overcome the influence of the obstacle via climbing. Once doing so, the dislocations can then glide on the new slip plane. However, the time spent by gliding between obstacles is significantly less than the time spent during the climb process and therefore climb controls the rate. Plastic deformation on the other hand is associated with dislocation glide and cross slip. Therefore, to recognise the combination of the two phenomena, a superposition of power laws is used, one that is relatively rate insensitive (associated with dislocation glide and cross slip), and the other rate sensitive (associated with dislocation climb). This modification is aimed at recognising that dislocation climb is a major rate controlling step, a modification also postulated by [45, 53-55] and a concept utilised by [56]in dislocation dynamic simulations. The flow rule was therefore decomposed into two power laws as presented in Eq 11.

$$\dot{\gamma}^{\alpha} = \left[\dot{\gamma}_{0,1}\left(\frac{|\tau^{\alpha} - X^{\alpha}|}{g^{\alpha}}\right)^{n_1} + \dot{\gamma}_{0,2}\left(\frac{|\tau^{\alpha} - X^{\alpha}|}{g^{\alpha}}\right)^{n_2}\right] sgn(\tau^{\alpha} - X^{\alpha}) \tag{11}$$

where $\dot{\gamma}_{0,1}$ and $\dot{\gamma}_{0,2}$ are the reference strain rate for dislocation glide and climb respectively, while n_1 and n_2 are the strain rate sensitivities for dislocation glide and climb respectively.

The authors recognise that there will also be a grain size dependence on the evolution of the slip hardening represented as g^{α} which the current constitutive model does not consider. Additionally, in the presented constitutive model development, the evolution of g^{α} is the same in both the plasticity and creep regimes. However, the evolution of g^{α} in the plasticity regime has the potential to be evolving differently from the creep regime. It is the intention of future work to consider these modifications.

2.3.3 Recovery

The final modification to the flow rule is the addition of a recovery term to the slip hardening equation. The formulation of the recovery term is determined based on the previous theoretical work on competing effects of work hardening and recovery occurring in metals [57, 58], where

recovery is associated with dislocation climb and dislocation annihilation [59]. Using the formulation provided in [60], the flow stress of the material (σ_0) is a function of both hardening and recovery, which can be expressed as,

$$\dot{\sigma_0} = h\dot{\varepsilon} - r \tag{12}$$

where h is the hardening and r the recovery. For the application to the crystal plasticity, the flow stress (σ_0) in Eq 12, is replaced in this case with g^{α} to represent the overall slip hardening evolution and therefore dislocation interactions, which follows the approach by Gittus [61] to recognise that the current flow stress is a function of the current dislocation density,

$$\dot{g^{\alpha}} = h\dot{\gamma^{\alpha}} - r \tag{13}$$

The hardening component defined by h is incorporated using Eq 7. The recovery component can be derived by applying the following as suggested by Evans and Wilshire [62],

$$r \propto v g^{\alpha d} \tag{14}$$

where v is the mobility of the climbing dislocation segments, and d is a power to control the influence of the evolution of slip hardening. To incorporate the temperature dependence on the recovery component, thus ensuring the magnitude of recovery is dependent on the temperature, the process outlined in Evans and Wilshire [62] was used where the dependence on v is characterised by an activation energy giving the following relationship,

$$r = A g^{\alpha d} \exp\left(-\frac{Q}{RT}\right) \tag{15}$$

where A is a fitting parameter, Q is the activation energy for creep, T is the temperature, and R is the universal gas constant.

Substituting the hardening component in Eq 7 and the recovery component in Eq 15 into Eq 13 gives the following final formulation which defines the complete hardening and recovery evolution,

$$\dot{g^{\alpha}} = h_0 \sum_{\beta=1}^{N_s} \left\{ \left(1 + \frac{h_0 \gamma_{sum}}{\tau_0 m}\right)^{m-1} \left|\dot{\gamma}^{\beta}\right| \right\} - A g^{\alpha d} \exp\left(-\frac{Q}{RT}\right) \tag{16}$$

From Eq 16, the recovery component includes the total value of slip hardening (g^{α}), which suggests that the magnitude of the recovery is dependent on the current amount of slip hardening, where more recovery processes have greater potential to occur with increased dislocation accumulation.

3.Experimental data

3.1 Material

Experimental data was extracted from the work by [31-33] and [9, 63] using 316H stainless steel loaded at 550°C.

3.2 Loading Conditions

Different loading conditions were used in the calibration and validation of the model. These included single strain-dwell loading in addition to a multiple strain dwell loading conditions. Details of the different single strain-dwell loading conditions used in the study are listed in Table 1, with a schematic of the type of loading provided in Figure 1. The experimental data used to compare against the simulation results was obtained from [31-33].

Load-up stress (MPa)	Strain dwell time (hours)
250	1,055
246	26
230	14,310

Table 1 Summary of single dwell stress relaxation tests considered in the study which are schematically demonstrated in Figure 1. The experimental data used to compare with simulations from [31-33].

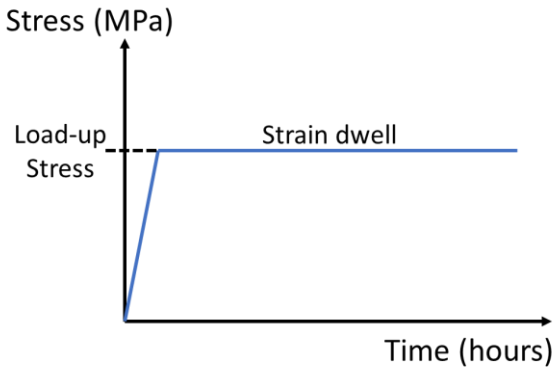

Figure 1 Schematic of the single strain dwell used in calibration and validation simulations.

The multiple strain dwell loading condition is schematically demonstrated in Figure 2, with information on the stress loadings and dwell times provided in Table 2. The experimental data used for this investigation was from [9, 63].

Loading sequence	Stress at the start of strain dwell (MPa)	Strain dwell time (sec)
1st load-up	95.0	3303
2nd load-up	155.6	3170
3rd load-up	191.9	4639
4th load-up	209.9	740
5th load-up	257.8	2460
6th load-up	270.7	3430
7th load-up	321.1	3120
8th load-up	364.0	2320

Table 2 Further information on the values of the load-up stresses and strain dwell times used in the multiple dwell loading sequence, as schematically represented in Figure 2. Experimental data sourced from [9, 63].

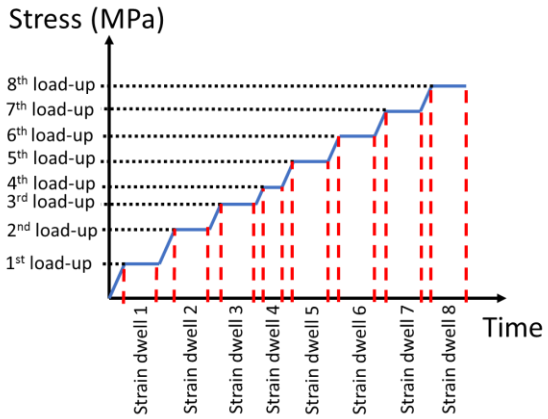

Figure 2 Schematic of the multiple strain dwell loading scenario used in the model validation simulations. Further information on the load-up stresses and time periods used in the strain dwells is provided in Table 2.

4. Finite Element Implementation

In the following sections the details of the approach taken to construct the representative volume is described followed by the details of the of the finite element model. It is also important to outline some of the assumptions made during the construction of the FE model. The dimensions of the model considered is on the meso-scale, which is the scale that lies between the macroscopic and atomistic [64], since the approach considers the influence of local effects such as dislocations, but does so by applying an average across the grain rather than modelling them individually. Additionally, the approach taken in the development of the FEM does not consider grain boundary sliding which has been found to have a more profound effect for materials with much smaller grains than being modelled in this study [65, 66].

4.1 Representative Volume Construction

The representative volume was built synthetically using DREAM.3D [67] during which a random texture was assigned to the grains within the volume. The final synthetic microstructure is provided in Figure 3, comprising of 226 grains. Since 316H stainless steel is a face centred cubic (FCC), slip was modelled to occur on 12 systems ($\{111\} < 110 >$).

The RVE was then meshed using 8-node linear brick elements (C3D8), totalling to 32,768 elements.

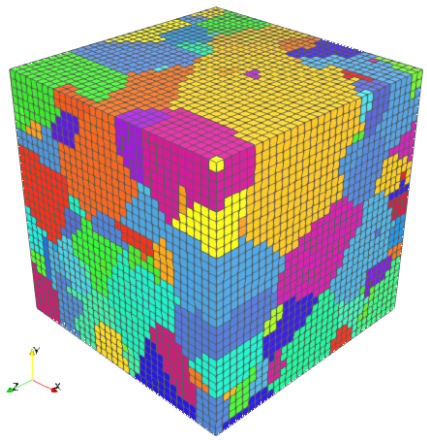

Figure 3 The RVE created using DREAM.3D where the colours represent different grains within the volume.

The grain diameter distribution extracted from EBSD data and which was also sampled during the synthetic build of the RVE is provided in Figure 4. The grain size comparison between that extracted from EBSD data and from the RVE is made using the equivalent spherical diameter. The equivalent spherical diameter of the RVE grains is calculated using the volume of a single voxel and multiplying by the total number of voxels which form the grain resulting in total voxel volume for each grain (V). Using the total grain volume (V), the equivalent spherical diameter can be calculated using the following relationship,

$$D_{3D} = \sqrt[3]{\frac{6V}{\pi}} \tag{17}$$

The comparison provides confidence that the RVE contains a distribution of sizes which follows the same trend as that seen experimentally.

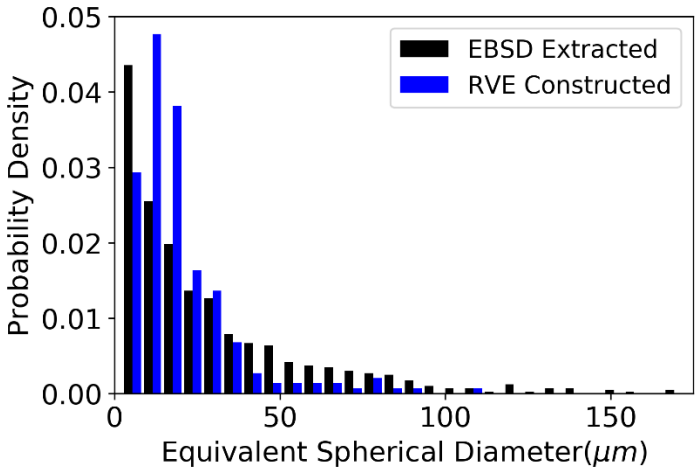

Figure 4 Comparison of the distributions of the grain sizes extracted from the EBSD scans and that contained with the constructed RVE.

4.2 Finite Element Analytical Details

The constitutive relations were implemented by modifying a user-defined material subroutine (UMAT) developed originally by Huang [39]. To solve for an increment in slipping rate ($\dot{\gamma}^{\alpha}$) an implicit time integration scheme ($\Delta\gamma^{\alpha} = \Delta t\dot{\gamma}_{t+\Delta t}$) was employed and the Newton-Raphson iterative method to solve the nonlinear equations was used (details of the modification and implementation of this approach is given in Appendix A). The implemented elasto-plastic tangent stiffness matrix used by the finite element solver during the iteration procedure was derived by Huang [39]. All simulations were conducted using the finite element code ABAQUS/Standard [68].

The maximum time increments used in the simulations are listed in Table 3. The tensile load refers to the loading during which an incrementally increasing stress or strain is applied to the model.

Table 3 Time increments used in the different loading conditions used in this study.

Load Case	**Maximum Time Increment(secs)**
Tensile	0.05
Strain Dwell (>10,000 hours)	100,000
Strain Dwell (<1000 hours)	100
Load Dwell	10,000

The boundary conditions employed are important in ensuring the RVE deformation is representative of the macro-scale behaviour. This is achieved by assuming symmetry, through the application of the boundary conditions as motivated by [69-72] and demonstrated in Figure 5.

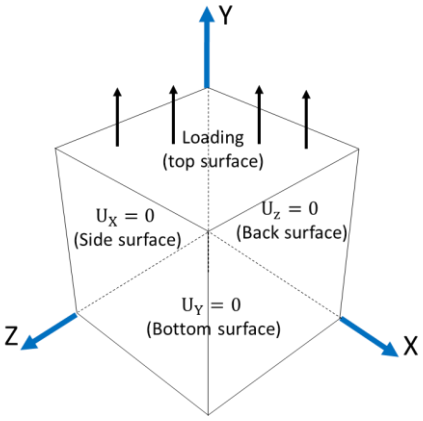

Figure 5 Surface breakdown of the RVE to demonstrate the application of boundary conditions.

To obtain the global stress-strain response of the RVE, an averaging method used by Kashinga, Zhao, Silberschmidt, Farukh, Barnard, Whittaker, Proprentner, Shollock and McColvin [73] was employed, which uses volume integrals,

$$\overline{\sigma_{ij}} = \frac{1}{V_T}\int \sigma_{ij} dV \quad , \qquad \overline{\varepsilon_{ij}} = \frac{1}{V_T}\int \varepsilon_{ij} dV \tag{18}$$

where $\overline{\sigma_{ij}}$ and $\overline{\varepsilon_{ij}}$ are the average stress and strains respectively, which represents the global response, V_T is the total volume of the RVE, V is the element's volume and σ_{ij} and ε_{ij} are the local stresses and strains. To compute the integral, the local stress, strains and volume were obtained from integration points of each element in ABAQUS. A post-processing Python script was developed and used to access the results from the ABAQUS output file (odb file) to complete the averaging method across all integration points in the model and arrive at a global response.

5. Parameter Calibration

In the following sections the methods used to calibrate the parameters adopted in the constitutive models is presented. The total number of parameters which require calibration against experimental data are eleven $(h_o, \tau_0, m, \dot{\gamma}_{0,1}, \dot{\gamma}_{0,2}, n_1, n_2, d, A, h, h_D)$ and six other parameters are directly measured $(c_{11}, c_{12}, c_{44}, Q, R, T)$. As much detail as possible is given to describe each of the processes undertaken to determine these values in order to provide ease of implementation to anyone endeavouring to use these constitutive models for different material. Additionally, the approach given makes use of only two data sets for successful calibration of the parameters, allowing for ease of application of the presented model.

5.1 Strain Hardening and Kinematic Hardening Parameters

The slip hardening parameters were calibrated by fitting to tensile stress-strain experimental data obtained from experiments using 316H stainless steel at 550°C by [9, 63], with the kinematic hardening component initially set to zero. This was done to evaluate the hardening modulus parameter h_0. The value of h_0 was optimised to fit the stress-strain evolution beyond yield and, since τ_o controls the initiation of slip, this value was altered to provide an accurate initial yield strength. To ensure the modelling capability of the stress-strain evolution for large strains was accurate, the experimental stress-strain evolution extracted from the stress (and corresponding strain) at the start of each dwell in [9, 63] was used. The final parameters provide a good fit to the experimental tensile stress-strain data.

Once the strain hardening (isotropic hardening) component was determined, the kinematic component could then be incorporated. To provide an initial estimate of the AF parameters, a calibration process was created. Using experimental data from [6], the first cycle from symmetric strain-controlled tests at a strain range of $\pm 0.6\%$ with R=-1 were extracted and the total intergranular and intragranular stress were calculated using Cottrell's method [74] to estimate the total back-stress. The total kinematic (X) and isotropic hardening (R) were estimated using Cottrell's method by probing different locations on the hysteresis loop as demonstrated in Figure 6 where σ_{eff} is the effective stress which is a combination of the yield stress (σ_y) and the isotropic hardening ($\sigma_{eff} = R + \sigma_y$).

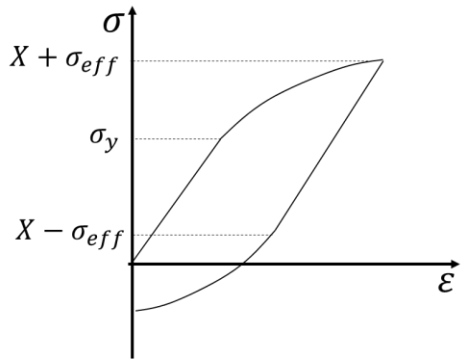

Figure 6 A schematic demonstrating Cottrell's method [74] to provide an estimate to the magnitude of kinematic hardening (X), which was then used to estimate the parameters which control the magnitude of intragranular residual stress.

Applying this approach leads to a total back-stress of 118MPa, which provides an upper bound on the saturated value of intragranular residual stress evolving according to Eq. 10 . Starting with this value, monotonic simulations could be undertaken and compared to the experimental stress-strain evolution. Since this value is the combination of both intergranular and intragranular stresses, the values of h and h_D in Eq. 10 were then manipulated to reduce the magnitude of the ratio h/h_D to incorporate the intergranular residual stresses inherent to the CPFE. Additionally, the isotropic component was also reduced slightly to allow for the introduction of the kinematic component since the isotropic parameters were developed assuming no kinematic hardening. This was done by also reducing the size of h_0. This approach of developing synergy between the two hardening phenomena was undertaken until the simulation results matched the experimental data as closely as possible, with the final results given in Figure 7.

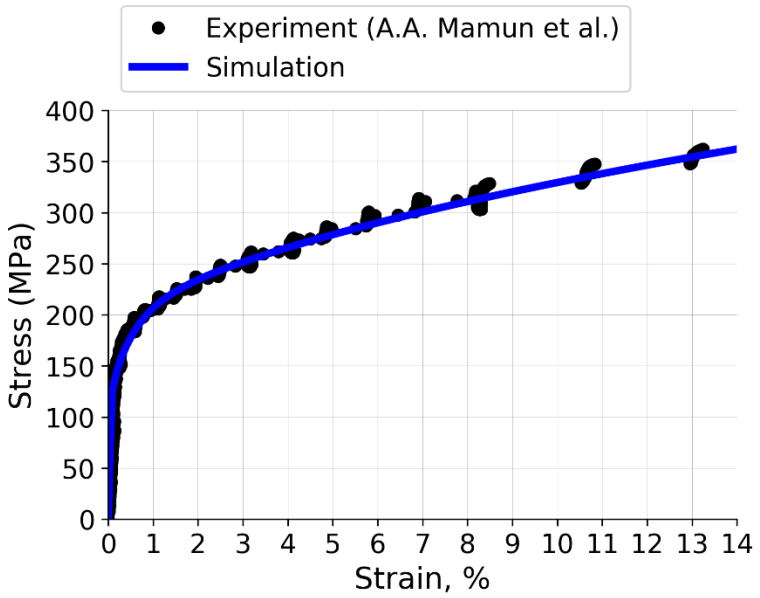

Figure 7 Stress-strain evolution of 316H at 550°C from low to high strain under tensile loading.

5.2 Slip Rate Parameters

The parameters for the slip rate during the loading phase dominated by glide were based on the assumption that the evolution of glide should only dominate during the plastic regime thus a large value for the power (n_1) was required. The final value for n_1 was arrived at by balancing the need to ensure the evolution of slip due to dislocation glide had limited influence during the dwells, but also was not too large a value to create issue with convergence (which has been shown to be a problem by Harewood and McHugh [75]).

The next focus was the values for the creep regime during which the creep power-law in the constitutive model is the more dominant. In this regime, the simulation requires a far slower slip rate than that occurring in the plasticity regime, therefore, a significantly smaller value for reference strain rate is required than that used to in the plasticity power law. Additionally, the sensitivity of evolution of slip can be adjusted by controlling the size of the strain rate sensitivity parameter (n_2). To develop the values of $\dot{\gamma}_{0,2}$ and n_2 to effectively simulate the evolution of slip during initial dwell, the strain dwell experimental results from [31, 32] at 230MPa at a temperature of 550°C were used with focus on the early stage of slip evolution (<200 hours). The values for $\dot{\gamma}_{0,2}$ and n_2 were then optimised to provide a good fit to the experimental data, with the results given in Figure 8.

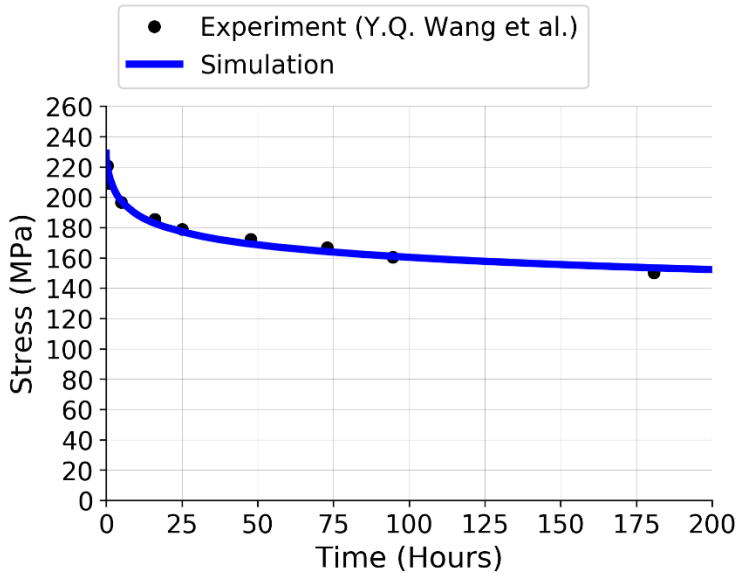

Figure 8 The final calibrated fit to the early stages of the stress relaxation using data gathered from [31, 32]. This calibration is used to arrive at the correct values for $\dot{\gamma}_{0,2}$ and n_2.

5.3 Recovery Parameters

The parameters defining the recovery process were calibrated from experimental data from long (>1000 hours) load or strain dwell tests during which the recovery is more dominant. Firstly, the activation energy was taken as the average across the expected stress range as given by Kloc, Skienička and Ventruba [76]. The value of d in Eq 16 could firstly be estimated from the understanding that for intermediate/high stress and temperatures from ~ 0.4 to $0.7T_m$ its value should be approximately 3 or greater [62]. Therefore, using the value of 3 as a starting point, the values of d and A could be adjusted to ensure the recovery evolves effectively enough to provide a good fit to long dwells (simulating the stress relaxation beyond approximately 1000 hours). In this work, a strain dwell was used as the calibration data, by once again using the experimental data with a maximum stress of 230MPa at a temperature of 550°C gathered by [31, 32]. d and A were then adjusted to provide a good fit to this data beyond approximately 1000 hours with the final fit provided in Figure 9.

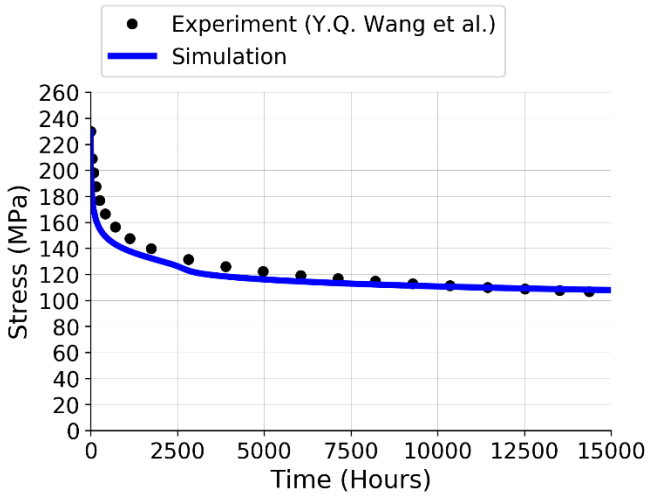

Figure 9 The final calibrated fit to the later stages (>1000 hours) of stress relaxation using data gathered from [31, 32].

The final and complete set of parameters used in simulations are listed in Table 4 (with the parameters derived in this work the following: $h_o, \tau_0, m, \dot{\gamma}_{0,1}, \dot{\gamma}_{0,2}, n_1, n_2, d, A, h, h_D$).

Table 4 Final material parameters used in simulations.

Equation	Parameters	Value
Elastic modulus	c_{11}, c_{12}, c_{44}	183.9 GPa, 123.4GPa, 91.5GPa
Slip hardening	h_o, τ_0, m	500MPa, 45MPa, 0.35
Slip rate	$\dot{\gamma}_{0,1}, \dot{\gamma}_{0,2}, n_1, n_2$	$1s^{-1}$, $3\times 10^{-8}s^{-1}$, 500, 10
Recovery	Q, R, T, d, A	418KJ/mol, 8.31J/mol K, 823K, 3, 3×10^{16}
Type III residual stress	h, h_D	6555MPa, 245

6. Macro-Scale and Meso-Scale Prediction Results

6.1 Macro-scale prediction/validation

The model prediction is compared with the experimental results for loading containing multiple strain dwells in Figure 10. From the results, it is evident that the model in combination with the parameter calibration procedure produces very accurate simulation results. The simulation accurately recognises the stress relaxation for each of the dwells with the rate of relaxation being well predicted. The accuracy of the results is particularly evident in Figure 10 (b) which plots each strain dwell separately.

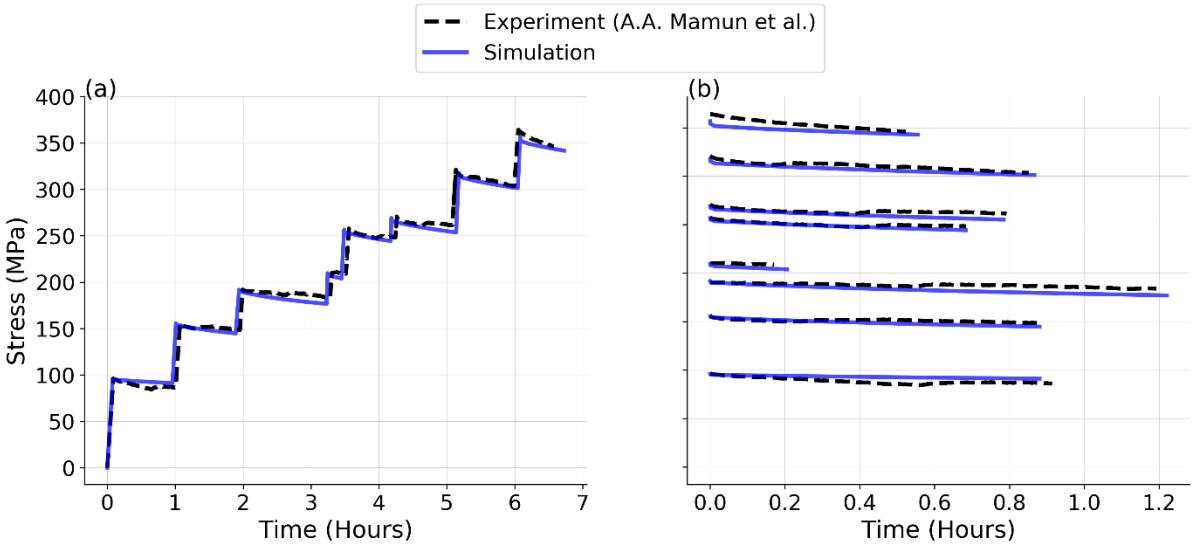

Figure 10 Simulation results achieved for the multiple strain dwell loading case where (a) shows the complete loading history and (b) displays the results for each individual dwell to provide further clarity of the achieved simulation accuracy.

In order to consider the influence of the relaxation component of the slip hardening and to further validate the model, another single strain dwell loading case was considered. The results of the simulation compared to experimental data is provided in Figure 11, which shows the simulation once again being in good agreement with the experimental results. The relaxation rate during the early stages (<100 hours) (Figure 11 (a)) of the dwell is very well simulated, which suggests that the model's evolving shear strain when averaged across all the grains within the RVE is progressing at a rate representative of that occurring during the dwell. Additionally, the gradual saturation of the evolving strain at the later stages of the dwell (>500 hours) (Figure 11 (b)) is also well captured by the model which indicates that the recovery component of the slip hardening formulation is activating correctly to ensure the saturation of the shear strain is also representative of that occurring in the material. This provides further support to the importance of the modifications made to the constitutive models.

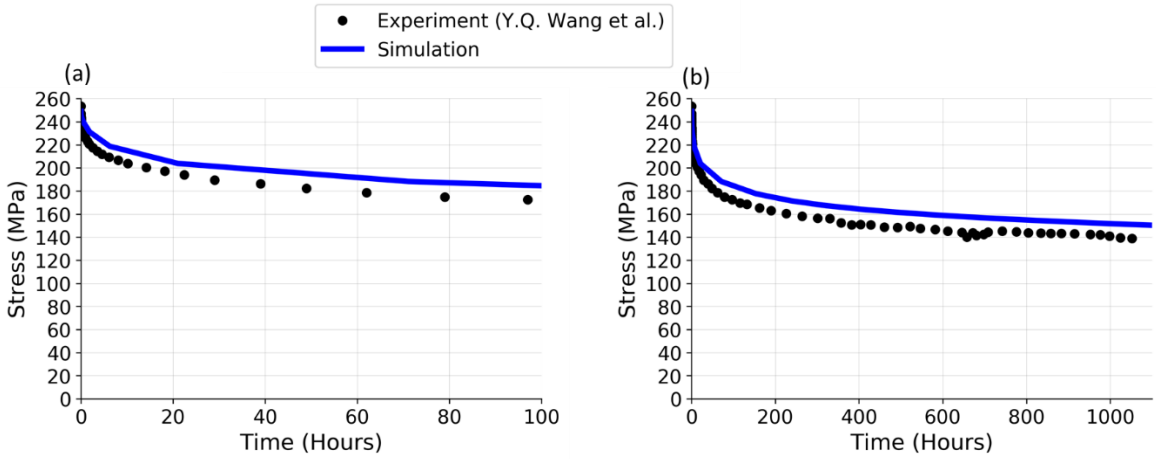

Figure 11 Comparison of the simulated response of the stress relaxation during a single strain dwell compared to the experimental data from [31, 32].

6.2 Meso-scale prediction/validation

With the developed constitutive models giving accurate macro-scale results, meso-scale information was then interrogated to make full use of the CPFE. This level of interrogation compliments experimental findings, since it provides an opportunity to investigate grains and their environment and how these contribute to the development of localised damage. One area of interest the CPFE could provide deeper insight into is the creep inhomogeneity reported to occur during creep by [9, 11]. Similar to plastic anisotropy during load-up, creep inhomogeneity is a phenomena also associated with grain-to-grain interactions, but instead refers to grain-to-grain interactions occurring due to different creep rates between grains [9, 63]. Additionally, creep inhomogeneity is influenced by prior plastic loading since different levels of plastic deformation occurring between families during initial loading has potential to also influence the heterogeneity of creep strain accumulation in the grain families during subsequent creep [9, 63].

The creep inhomogeneity can be visualised by calculating the ideal elastic lattice strains during the dwells and determining whether the lattice strains are deviating from these ideal elastic values. The ideal elastic strains are calculated using the macro-scale stress relaxation and the diffraction elastic constants determined by Wang, Hossain, Kabra, Zhang, Smith and Truman [33] in conjunction with the following relationship,

$$\varepsilon_{hkl} = \frac{\sigma}{E_{hkl}} \tag{19}$$

where ε_{hkl} is the ideal elastic strain for the [25] grain family, E_{hkl} is the elastic modulus for each grain family, and σ is the macro-scale stress.

Neutron diffraction experiments were undertaken by Wang, Hossain, Kabra, Zhang, Smith and Truman [33], who investigated the influence of elastic follow-up on lattice strain evolution during creep. Elastic follow-up is a term used to describe the influence of a global elastic environment on localised regions undergoing plastic deformation [77]. With increasing levels of elastic follow-up, the loading transitions from displacement control to stress control loading. The amount of

elastic follow-up can be quantified by an elastic follow-up factor Z [33], where Z=1 is displacement control, and Z=∞ is stress control.

To investigate the influence of elastic follow-up on the creep inhomogeneity in the material, the developed CPFE was used to simulate the lattice strain evolution during a strain dwell containing no elastic follow-up to compare against the Wang, Hossain, Kabra, Zhang, Smith and Truman [33] experimental results containing a small amount of elastic follow-up (Z=1.2). In order to make this comparison, the same load-up conditions as that applied by Wang, Hossain, Kabra, Zhang, Smith and Truman [33] for the Z=1.2 case was simulated, which involved loading up in tension to a stress of 246MPa and holding the strain for a period of approximately 26 hours, as summarised in Table 1.

To compare simulated lattice strain against the experimental values, the process used to extract the lattice strains for each family from the CPFE model required determining which grains within the RVE have {*hkl*} planes orientated to contribute to diffraction. To do this, the normal vector to the {*hkl*} planes in the local lattice coordinate system was calculated as follows,

$$\boldsymbol{N}_{hkl} = \frac{(h\boldsymbol{e}_1 + k\boldsymbol{e}_2 + l\boldsymbol{e}_3)}{\sqrt{h^2 + k^2 + l^2}} \tag{20}$$

where $\boldsymbol{e}_1$, $\boldsymbol{e}_2$, $\boldsymbol{e}_3$ are the orthogonal vectors of the local lattice configuration.

The normal of the plane in the global coordinate system ($\boldsymbol{n}_{hkl}$) was then obtained by rotating the normal in the local lattice configuration ($\boldsymbol{N}_{hkl}$) using the rotation matrix ($\boldsymbol{R}$) based on the Euler orientation angles (φ_1, Φ, φ_2) describing the orientation of the grain. The rotation matrix is formed by combining three successive rotations based on the convention of Bunge, where the rotations are first around the Z axis, then X axis, and finally around the new Z axis. This results in the following matrix,

$$\boldsymbol{R} = \begin{bmatrix} \cos\varphi_1 \cos\varphi_2 - \cos\Phi \sin\varphi_1 \sin\varphi_2 & \sin\varphi_1 \cos\varphi_2 + \cos\Phi \cos\varphi_1 \sin\varphi_2 & \sin\Phi \sin\varphi_2 \\ -\cos\varphi_1 \sin\varphi_2 - \cos\Phi \sin\varphi_1 \cos\varphi_2 & \cos\Phi \cos\varphi_1 \cos\varphi_2 - \sin\varphi_1 \sin\varphi_2 & \sin\Phi \cos\varphi_2 \\ \sin\Phi \sin\varphi_1 & -\sin\Phi \cos\varphi_1 & \cos\Phi \end{bmatrix} \tag{21}$$

The normal in the global coordinate system was then calculated using the following relationship,

$$\boldsymbol{n}_{hkl} = \boldsymbol{R}^T \boldsymbol{N}_{hkl} \tag{22}$$

The angle between the diffraction vector ($\boldsymbol{g}$) and the plane normal defined in the global coordinate system ($\boldsymbol{n}_{hkl}$) was then calculated using the following,

$$\theta = \cos^{-1} \frac{(\boldsymbol{n}_{hkl} \cdot \boldsymbol{g})}{(|\boldsymbol{n}_{hkl}| \cdot |\boldsymbol{g}|)} \tag{23}$$

The grain from which the lattice strains were extracted was chosen if the calculated angle between the two vectors (θ) was within a specified tolerance of $\pm 7.5°$ to be consistent with the process used for extracting the experimental data, in addition to ensuring enough grains were averaged across.

The average lattice strain across each individual grain with $\{hkl\}$ planes oriented within the tolerance specified was calculated using the following formulation,

$$\overline{\varepsilon_{ij}} = \frac{1}{V_T}\int \varepsilon_{ij} dV \tag{24}$$

where $\overline{\varepsilon_{ij}}$ are the average lattice strain across the grain, V_T is the total volume of the grain, V is the element's volume and ε_{ij} is the element lattice strain.

The lattice strain evolution of the family was then calculated by taking the average response across all identified grains within the $\pm 7.5°$ tolerance according to the following equation,

$$\varepsilon_{hkl} = \frac{\sum_{N=1}^{N_{grain}} \overline{\varepsilon_{ij}}}{N_{grain}} \tag{25}$$

where ε_{hkl} is the lattice strain for the $\{hkl\}$ planes, and N_{grain} is the number of grains identified to be within the $\pm 7.5°$ tolerance.

The following simulations were undertaken without modification of parameters listed in Table 4. Firstly, the macro-scale tensile stress-strain evolution between the experimental results reported by Wang, Hossain, Kabra, Zhang, Smith and Truman [33] and the those simulated by the model were compared to ensure the modelling capability could accurately predict the macro-scale results. This was a necessary step to validate the overall accuracy of the model before extracting information on the meso-scale. The simulation and experimental tensile results are compared in Figure 12, with the results being in good agreement, validating the use of the developed CPFE model to investigate grain-level deformation.

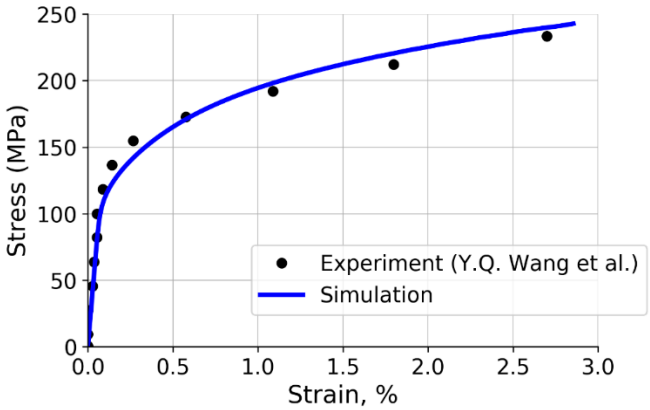

Figure 12 Comparison of the simulated and experimental tensile results from [33] for 316H stainless steel at 550°C

Applying the method outlined to extract grain average responses for each family from the CPFE, the lattice strains for the {111}, {200}, {311}, and {220} families in the longitudinal direction during load-up were extracted and compared to the lattice strain evolution experimentally determined by Wang, Hossain, Kabra, Zhang, Smith and Truman [33]. The comparisons are made in Figure 13.

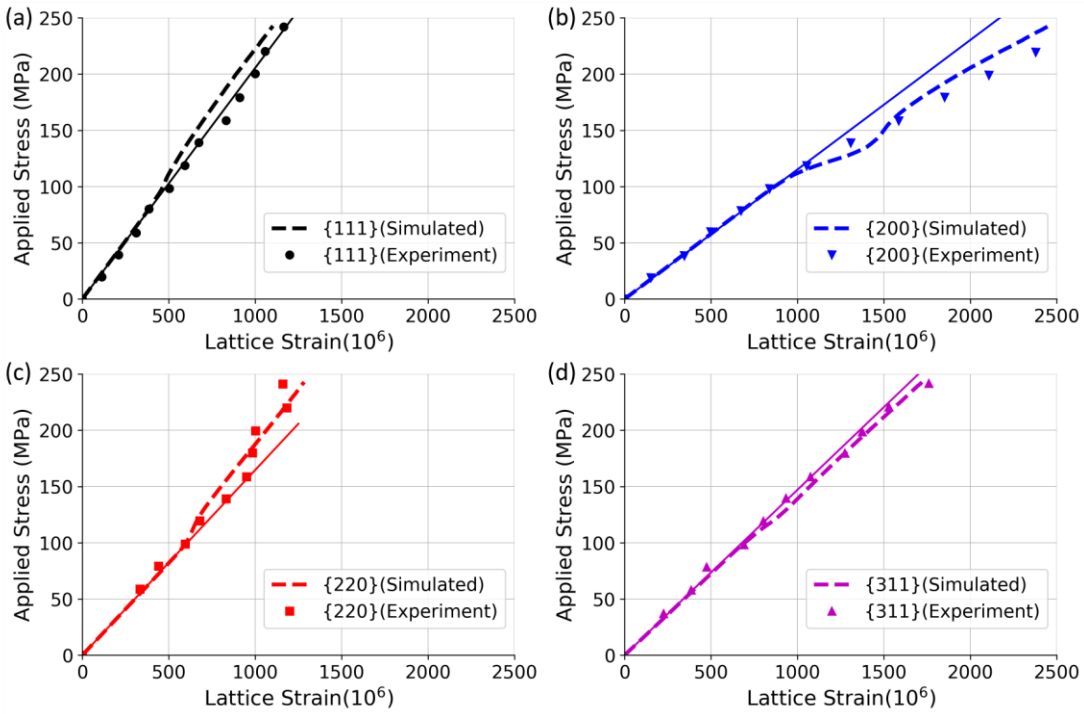

Figure 13 Experimental longitudinal lattice strain evolution from [33] for grain families (a) {111}, (b) {200}, (c) {220}, and (d) {311} compared to simulated lattice strain evolution.

The simulation results for the families compare well with the extracted experimental results from Wang, Hossain, Kabra, Zhang, Smith and Truman [33]. In addition to the lattice strain evolution, the ideal elastic line (using Eq 19) was also added to each figure to demonstrate the deviation of the lattice strain from elastic conditions, therefore, highlighting the relative amount of intergranular stress and strain within grain families. The ability of the model to predict the intergranular stress evolution during plasticity is therefore confirmed by the results with the lattice strain evolution within the grain families showing comparatively similar behaviour to that seen in the experimental data, particularly in grain families {220} and {200} which show very accurate deviation from the ideal elastic line. This provides greater confidence in the simulated interaction of the grains within the model, by accurately considering the internal push and pull between grains associated with the influence of plastically deforming grains on grains still elastically deforming [9, 63].

The relaxation in lattice strains occurring during the dwell for each family were extracted and compared to the experimental results in Figure 14. In Figure 14, the strains for each family were normalised with respect to the maximum strain within each family. Doing so ensures the lattice strain evolution for each family starts from zero, allowing for ease of comparison in evolution. Also included in the figure is a line of best fit to provide a better visual representation of the trend of the data. The simulated lattice strains are comparable with the experimental results with the magnitude in relaxations between families showing the same trend as that in the experimental case, where the magnitude of relaxation is greatest in the {200} family and the least in the {111} family.

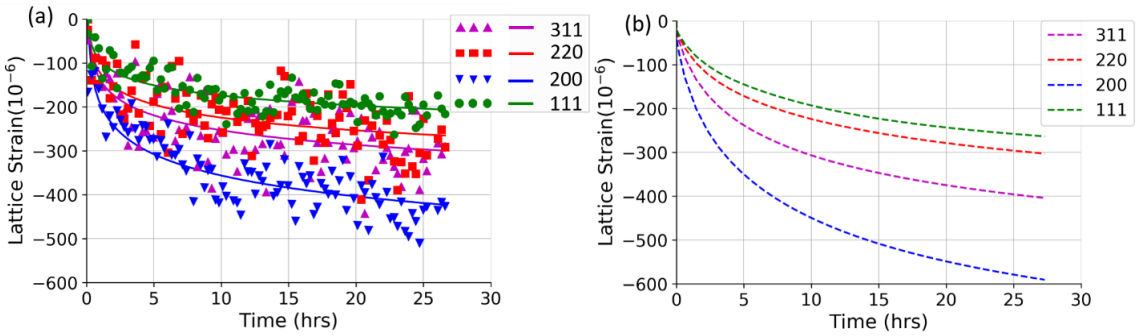

Figure 14 Comparison of the lattice strain relaxation for each grain family between the experimental results (from [33]) (a) and the simulation results (b).

A more detailed comparison of the simulated and experimental lattice strain relaxations is provided in Figure 15 between grain families.

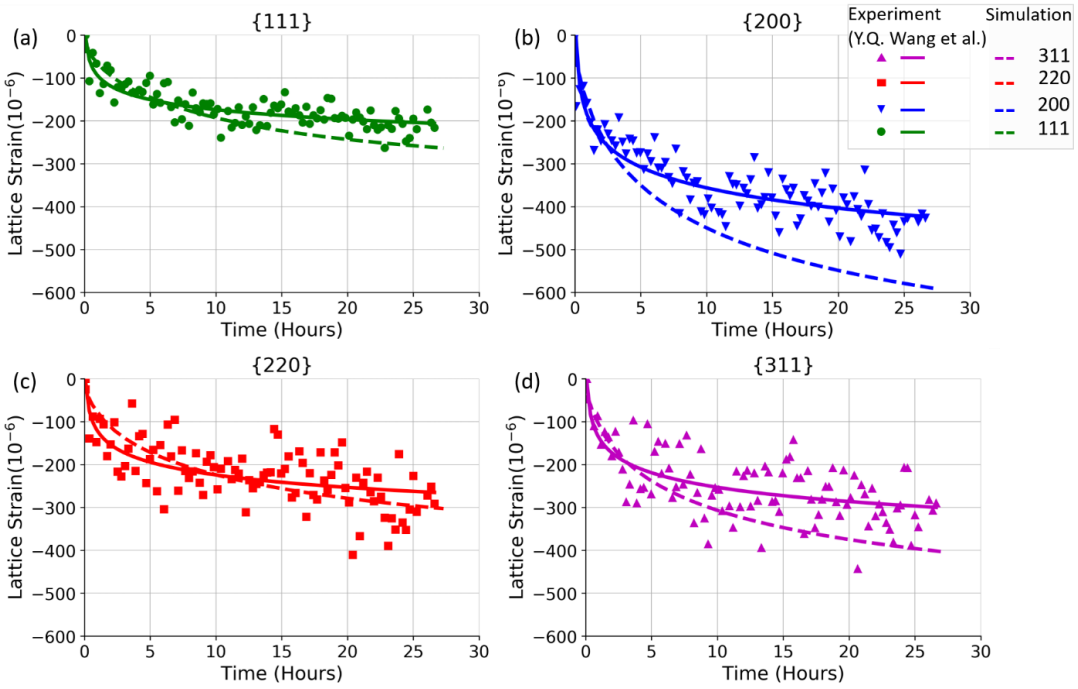

Figure 15 Experimental and simulation comparison of the relaxation of lattice strain for each family (a) {111} (b) {200} (c){220} (d) {311}.

Closer inspection of the evolution of the lattice strain highlights the accuracy in the {111} and {220} predicted magnitudes. In the {200} and {311} families the predicted evolution is quite accurate within the 5-hour window of the dwell before a slight divergence between the experiment and simulation occurs with continued holding. This difference could be the consequence of the influence of elastic follow-up. Due to the difficulty in accurately simulating the elastic follow-up, an approximation approach could be applied by recognising that there is an accumulated creep strain within the material due to elastic follow-up which will further decrease the creep stress relaxation rate [32]. Therefore, the simulated relaxation curves were

adjusted accordingly (by adjusting the magnitude by 1.2) to investigate the potential influence of elastic follow-up on the magnitude of lattice strain relaxation, with the results provided in Figure 16.

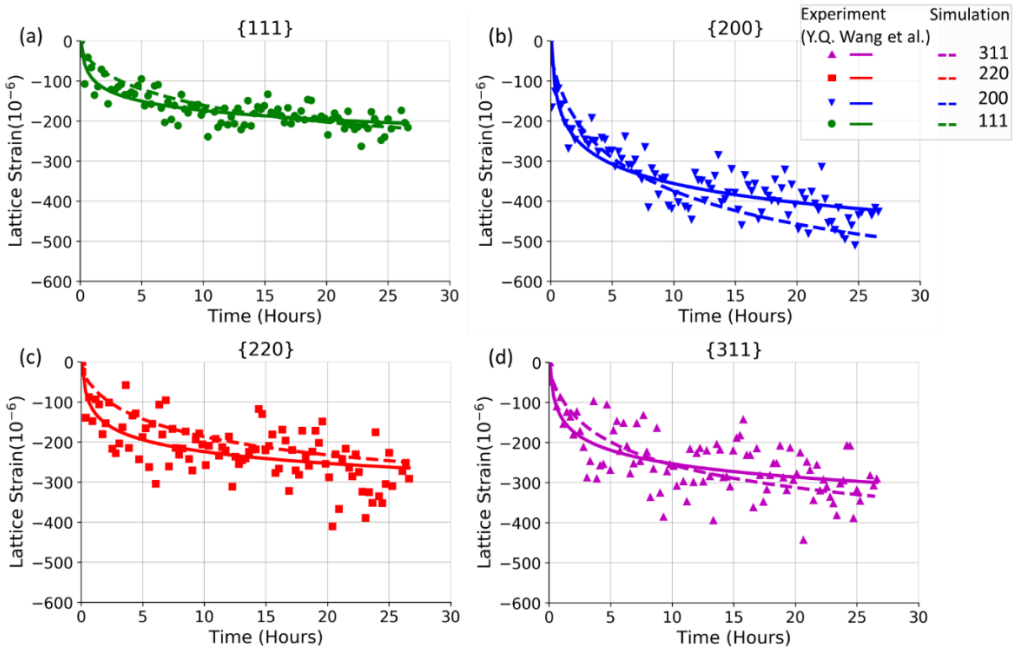

Figure 16 Experimental and simulation comparison of the relaxation of lattice strain with an adjustment to the magnitude of creep strain as an approximate recognition of Z=1.2 for each family (a) {111} (b) {200} (c){220} (d) {311}.

The approximate adjustment of the relaxation magnitude for each family to recognise the small elastic follow-up improves the simulation results for all four families, with the magnitude in relaxation in good agreement with the experimental relaxation.

7. Discussion

The simulation results achieved during the macro-scale validation indicates that separating the shear strain evolution between the plasticity and creep regimes to recognise the differences in evolution is successful at achieving the desired effect. The results indicate a significant level of accuracy with success in simulating several different loading conditions. Furthermore, the seamless transition from plasticity to creep during the multiple dwells in Figure 10 further supports the approach to use a superposition of different power law relations. The prior deformation history is accurately captured and effectively used in subsequent load-ups and dwells, which suggests that the combined influence of the two power laws works effectively not only for a single load case but for more complex loading conditions where the prior deformation history will have an influence on future loading. This is a particularly important finding since it encourages the application of the presented constitutive model to further complex loading where accurate transitioning of deformation from the plasticity and creep regimes is required.

Such loading conditions include the influence of cyclic plasticity on creep strain, recently investigated computationally by [5, 30]. The importance of accurate prediction of these sort of conditions are of importance in thermal power plants where transient conditions can induce a local cyclic plasticity.

The accuracy of the proposed constitutive model is further supported by the meso-scale simulation predictions. Predicted lattice strain evolution during plasticity for all three families are in very good agreement with the experimental data. Plastic anisotropy is very well simulated with deviation from the ideal elastic lines for each family indicative of the behaviour noticed experimentally. This is especially evident in the {200} family which shows the greatest amount of plastic anisotropy, predictions displaying a similar magnitude.

The ability of the model to simulate the lattice strain evolution during creep was also investigated for the {111} and {200} families, the results demonstrating accurate amounts of relaxation when compared to the experimental data. Slight deviation in the predicted magnitudes of lattice strain from experimental results were noticed in the {200} and {311} families. This was hypothesised to be the consequence of the influence of elastic follow-up in the experiment. This hypothesis was investigated by applying an approximate adjustment to the magnitude of relaxation for each family to recognise the additional creep strain in the experiment that is not present in the simulation, as a consequence of the elastic follow-up in the experiment. Doing so improved the simulation accuracy of the magnitude in relaxation across all four tested families, which suggests that even a small amount of elastic follow-up had an influence on the magnitude of lattice strain relaxation in the tested grain families.

8. Conclusion

A constitutive model which combines the deformation evolution during both plasticity and creep has been presented. The conception of the model originates from the need to recognise the differing micromechanics occurring in the two regimes and the need to ensure the deformation with each of the regimes correctly influences the deformation of succeeding loading. The following conclusions can be drawn from this study:

1. The superposition of power laws to recognise the differing micromechanics occurring between the plasticity and creep regimes provided ease of transition to occur from plasticity to creep during the multiple dwell simulations. The accuracy in simulated relaxation for later dwells also highlighted the model's capability to recognise prior deformation on succeeding load cases.
2. Improvements in simulation accuracy of strain-dwells of 316H at 550°C were achieved through the addition of a recovery component to the evolution of slip hardening. Comparisons made between the experiments and simulation demonstrated the importance of balancing the hardening and recovery during long strain-dwells (>1000 hours).
3. A calibration procedure was introduced to encourage further application of the constitutive model developed during this study to other materials. The calibration procedure presented requires only limited data to achieve accurate simulation accuracy of load cases outside of those used for calibration on both the macro- and meso- scale, which highlights the robustness and applicability of the presented model

4. Meso-scale validation of the model highlighted its capability to simulate lattice strain evolution in both plasticity and creep, which further supports the presented superposition of power laws to simulate slip. Plastic anisotropy was successfully simulated for each grain family, with deviation from the ideal elastic line for each family showing the same trend and magnitude as that in the experimental data.

Data availability

The raw experimental data used to compare against simulation results can be obtained from [9, 31-33].

Acknowledgments

The authors would like to thank EDF Energy and EPSRC [grant EP/R020108/1] for funding this work. Additionally, the authors would like to thank the computational facilities of the Advanced Computing Research Centre, University of Bristol (http://www.bris.ac.uk/arc/), which was used for the simulation component of this study. Dr. Wang would also like to acknowledge the RCUK Energy Programme [grant EP/T012250/1] and the UK Government Department for Business, Energy and Industrial Strategy.

Appendix. A. Integration Scheme Applied to the Constitutive Relations

As outlined by Huang [39], the integration scheme implemented in the subroutine is the tangent modulus method for rate dependent solids proposed by Peirce, Shih and Needleman [78]. Firstly, the increment of shear strain within a time increment Δt is calculated as:

$$\Delta\gamma^{\alpha} = \gamma^{\alpha}(t+\Delta t) - \gamma^{\alpha}(t) \tag{A.126}$$

Employing a linear interpolation with Δt, the increment of shear strain can be calculated,

$$\Delta\gamma^{\alpha}_{t+\Delta t} = \dot{\gamma}^{\alpha}_{t+\Delta t}(\Delta\gamma^{\alpha}_{t+\Delta})\Delta t \tag{A.2}$$

where $\dot{\gamma}^{\alpha}$ is the slip rate in slip system α at time $t+\Delta t$ which is calculated using the following,

$$\dot{\gamma}^{\alpha}_{t+\Delta t} = \left[\dot{\gamma}_{0,1}\left(\frac{|\tau^{\alpha}_{t+\Delta t} - X^{\alpha}_{t+\Delta t}|}{g^{\alpha}_{t+\Delta t}}\right)^{n_1} + \dot{\gamma}_{0,2}\left(\frac{|\tau^{\alpha}_{t+\Delta t} - X^{\alpha}_{t+\Delta t}|}{g^{\alpha}_{t+\Delta t}}\right)^{n_2}\right] sgn(\tau^{\alpha}_{t+\Delta t} - X^{\alpha}_{t+\Delta t}) \tag{A.3}$$

The values for the resolved shear stress, type III residual stress and slip hardening/recovery can be calculated at $t+\Delta t$ once $\Delta\gamma^{\alpha}_{t+\Delta t}$ is known. Firstly, the slip hardening and type III residual stress can be calculated applying the following,

$$g^{\alpha}_{t+\Delta t} = g^{\alpha}_{t} + h_0 \sum_{\beta=1}^{N_s}\left\{\left(1+\frac{h_0\gamma_{sum(t+\Delta t)}}{\tau_0 m}\right)^{m-1}\left|\Delta\gamma^{\beta}_{t+\Delta t}\right|\right\} - A g^{\alpha h}_{t}\, exp\left(-\frac{Q}{RT}\right)$$
$$X^{\alpha}_{t+\Delta t} = X^{\alpha}_{t} + h\Delta\gamma^{\alpha}_{t+\Delta t} + h_D X^{\alpha}_{t}|\Delta\gamma^{\alpha}_{t+\Delta t}| \tag{A.4}$$

where the accumulated shear strain ($\gamma_{sum(t+\Delta t)}$) is calculated in the following way,

$$\gamma_{sum(t+\Delta t)} = \gamma^{\alpha}_{t} + \sum_{\alpha}|\Delta\gamma^{\alpha}_{t+\Delta t}| \tag{A.5}$$

The resolved shear stress at $t+\Delta t$ can also be calculated using the shear stress derived in Huang [39], which is given as,

$$\tau^{\alpha}_{t+\Delta \mathrm{t}} = \tau^{\alpha}_{t} + \left[L_{ijkl}\mu^{\alpha}_{kl} + \omega^{\alpha}_{ik}\sigma_{jk(t+\Delta t)} + \omega^{\alpha}_{jk}\sigma_{ik(t+\Delta t)}\right]\cdot\left[\Delta\varepsilon_{ij(t+\Delta t)} - \sum_{\beta}\mu^{\beta}_{ij}\Delta\gamma^{\beta}_{t+\Delta t}\right] \tag{A.6}$$

where L_{ijkl} is the elastic moduli, and μ^{α}_{ij} and ω^{α}_{ij} are given as,

$$\mu^{\alpha}_{\mathrm{ij}} = \frac{1}{2}\left[s^{*\alpha}_{i}m^{*\alpha}_{j} + s^{*\alpha}_{j}m^{*\alpha}_{i}\right]$$
$$\omega^{\alpha}_{\mathrm{ij}} = \frac{1}{2}\left[s^{*\alpha}_{i}m^{*\alpha}_{j} - s^{*\alpha}_{j}m^{*\alpha}_{i}\right] \tag{A.7}$$

To calculate the shear rate, Eq 6 must be solved for $\dot{\gamma}$ within an increment of time defined by the step size increment in the FE model. Since Eq 6 is a nonlinear equation containing function of resolved shear stress (τ^{α}), slip hardening strength (g^{α}) and type III residual stress (X^{α}), a

Newton-Raphson scheme was employed to solve for the current slipping rate within the specified time. To distinguish between $\Delta\gamma^{\alpha}$ and the Newton-Raphson iterated version, the $\boldsymbol{\Delta\gamma}^{k}$ is used where k represents the iteration of the Newton-Raphson algorithm. Therefore, the Newton-Raphson iteration is as follows,

$$\boldsymbol{\Delta\gamma}^{\boldsymbol{k+1}} = \boldsymbol{\Delta\gamma}^{k} - \frac{\boldsymbol{R}(\Delta\gamma^{\alpha}_{t+\Delta t})}{\frac{\partial \boldsymbol{R}(\Delta\gamma^{\alpha}_{t+\Delta t})}{\partial \boldsymbol{\Delta\gamma}}} \tag{A.8}$$

where the function to iteratively solve is as follows,

$$\boldsymbol{R}(\Delta\gamma^{\alpha}_{t+\Delta t}) = \Delta\gamma^{\alpha}_{t+\Delta t} - \dot{\gamma}^{\alpha}_{t+\Delta t}(\Delta\gamma^{\alpha}_{t+\Delta})\Delta t \tag{A.9}$$

The solution is arrived at once the following condition is met,

$$|\boldsymbol{R}(\Delta\gamma^{\alpha}_{t+\Delta t})| \leq TOL \tag{A.1027}$$

where the TOL in this study was taken as 1×10^{-6}.

The partial derivate of Eq A.9 with respect to the unknown increment in slip rate ($\partial \boldsymbol{R}(\Delta\gamma^{\alpha}_{t+\Delta t})/\partial \boldsymbol{\Delta\gamma}$) can be calculated using the following equation,

$$\frac{\partial \boldsymbol{R}(\Delta\gamma^{\alpha}_{t+\Delta t})}{\partial \boldsymbol{\Delta\gamma}^{\beta}} = \delta_{\alpha\beta} - \frac{\partial \dot{\gamma}^{\alpha}}{\partial \Delta\gamma^{\beta}}\Delta t \tag{A.11}$$

where $\delta_{\alpha\beta}$ is the Kronecker delta and the partial derivative of the slip rate can be solved following the expression,

$$\frac{\partial \dot{\gamma}^{\alpha}}{\partial \Delta\gamma^{\beta}} = \frac{\partial \dot{\gamma}^{\alpha}}{\partial \tau^{\alpha}}\frac{\partial \tau^{\alpha}}{\partial \Delta\gamma^{\beta}} + \frac{\partial \dot{\gamma}^{\alpha}}{\partial g^{\alpha}}\frac{\partial g^{\alpha}}{\partial \Delta\gamma^{\beta}} + \frac{\partial \dot{\gamma}^{\alpha}}{\partial X^{\alpha}}\frac{\partial X^{\alpha}}{\partial \Delta\gamma^{\alpha}} \tag{A.12}$$

Each of the partial derivatives of slip rate ($\dot{\gamma}^{\alpha}$) with respect to resolved shear stress, slip hardening and type III residual stress can be calculated as,

$$\frac{\partial \dot{\gamma}^{\alpha}}{\partial \tau^{\alpha}} = \frac{1}{g^{\alpha}}\left[\dot{\gamma}_{0,1}n_1\left(\frac{|\tau^{\alpha} - X^{\alpha}|}{g^{\alpha}}\right)^{n_1-1} + \dot{\gamma}_{0,2}n_2\left(\frac{|\tau^{\alpha} - X^{\alpha}|}{g^{\alpha}}\right)^{n_2-1}\right]$$

$$\frac{\partial \dot{\gamma}^{\alpha}}{\partial g^{\alpha}} = -\frac{|\tau^{\alpha} - X^{\alpha}|}{g^{\alpha 2}}\left[\dot{\gamma}_{0,1}n_1\left(\frac{|\tau^{\alpha} - X^{\alpha}|}{g^{\alpha}}\right)^{n_1-1} + \dot{\gamma}_{0,2}n_2\left(\frac{|\tau^{\alpha} - X^{\alpha}|}{g^{\alpha}}\right)^{n_2-1}\right] sgn(\tau^{\alpha} - X^{\alpha}) \tag{A.13}$$

$$\frac{\partial \dot{\gamma}^{\alpha}}{\partial X^{\alpha}} = -\frac{1}{g^{\alpha}}\left[\dot{\gamma}_{0,1}n_1\left(\frac{|\tau^{\alpha} - X^{\alpha}|}{g^{\alpha}}\right)^{n_1-1} + \dot{\gamma}_{0,2}n_2\left(\frac{|\tau^{\alpha} - X^{\alpha}|}{g^{\alpha}}\right)^{n_2-1}\right]$$

Additionally, the partial derivatives for the resolved shear stress, slip hardening and type III residual stress with respect to $\partial\Delta\gamma^{\beta}$ can be calculated as,

$$\frac{\partial \tau^{\alpha}}{\partial \Delta\gamma^{\beta}} = \sum_{\beta} \mu^{\beta}_{ij}\left[L_{ijkl}\mu^{\alpha}_{kl} + \omega^{\alpha}_{ik}\sigma_{jk} + \omega^{\alpha}_{jk}\sigma_{ik}\right] \tag{A.14}$$

$$\frac{\partial g^{\alpha}}{\partial \Delta\gamma^{\beta}} = h_0 \sum_{\beta=1}^{N_s} \left\{ \left(1 + \frac{h_0 \gamma_{sum(t+\Delta t)}}{\tau_0 m} \right)^{m-1} sgn\left(\Delta\gamma^{\beta}\right) \right\}$$

$$\frac{\partial X^{\alpha}}{\partial \Delta\gamma^{\beta}} = h\delta_{\alpha\beta} - h_D X^{\alpha} \delta_{\alpha\beta} sgn(\Delta\gamma^{\alpha})$$

Using the equations in Eq A.13 and Eq A.14, the partial derivative in Eq A.12 can be solved and finally, the value of $\boldsymbol{\Delta\gamma^{k+1}}$ can be solved.

References

[1] S. Tin, M. Detrois, J. Rotella, M.D. Sangid, JOM, 70 (2018) 2485-2492.
[2] C.C. Tasan, J.P.M. Hoefnagels, M. Diehl, D. Yan, F. Roters, D. Raabe, International Journal of Plasticity, 63 (2014) 198-210.
[3] S. Sinha, J.A. Szpunar, N.A.P. Kiran Kumar, N.P. Gurao, Materials Science and Engineering: A, 637 (2015) 48-55.
[4] G. Song, Z. Sun, L. Li, X. Xu, M. Rawlings, C.H. Liebscher, B. Clausen, J. Poplawsky, D.N. Leonard, S. Huang, Z. Teng, C.T. Liu, M.D. Asta, Y. Gao, D.C. Dunand, G. Ghosh, M. Chen, M.E. Fine, P.K. Liaw, Scientific Reports, 5 (2015).
[5] M.P. Petkov, J. Hu, A.C.F. Cocks, Philosophical Magazine, (2018) 1-46.
[6] T.D. Joseph, D. McLennon, M.W. Spindler, C.E. Truman, D.J. Smith, Materials at High Temperatures, 30 (2013) 156-160.
[7] S. Kikuchi, B. Ilschner, Scripta Metallurgica, 20 (1986) 159-162.
[8] A. Fookes, S.X. Li, D.J. Smith, M.W. Spindler, in: 2nd ECCC International Conference on Creep and Fracture in High Temperature Componets: Design and Life Assessment Issues, 2009.
[9] A.A. Mamun, C. Simpson, D. Agius, C. Reinhard, C. Truman, M. Mostafavi, D. Knowles, Acta Materialia, (In Review) (2019).
[10] A.A. Mamun, R.J. Moat, J. Kelleher, P.J. Bouchard, Materialia, 7 (2019) 100385.
[11] A. A. Mamun, R.J. Moat, J. Kelleher, P.J. Bouchard, Materials at High Temperatures, 31 (2014) 378-382.
[12] J. Hu, A.C.F. Cocks, International Journal of Solids and Structures, 78-79 (2016) 21-37.
[13] H. Wang, B. Clausen, C.N. Tomé, P.D. Wu, Acta Materialia, 61 (2013) 1179-1188.
[14] J.N. Hu, A.C.F. Cocks, Scripta Materialia, 128 (2017) 100-104.
[15] B. Chen, J.N. Hu, P.E.J. Flewitt, A.C.F. Cocks, R.A. Ainsworth, D.J. Smith, D.W. Dean, F. Scenini, Materials at High Temperatures, 32 (2015) 592-606.
[16] H. Wang, Y. Jeong, B. Clausen, Y. Liu, R.J. McCabe, F. Barlat, C.N. Tomé, Materials Science and Engineering: A, 649 (2016) 174-183.
[17] D.-F. Li, C.M. Davies, S.-Y. Zhang, C. Dickinson, N.P. O'Dowd, Acta Materialia, 61 (2013) 3575-3584.
[18] Y. Guilhem, S. Basseville, F. Curtit, J.M. Stéphan, G. Cailletaud, International Journal of Fatigue, 32 (2010) 1748-1763.
[19] L. Signor, P. Villechaise, T. Ghidossi, E. Lacoste, M. Gueguen, S. Courtin, Materials Science and Engineering: A, 649 (2016) 239-249.
[20] K. Minaii, G.H. Farrahi, M. Karimpour, H. Bahai, G.H. Majzoobi, Fatigue and Fracture of Engineering Materials and Structures, 42 (2019) 640-650.
[21] A. Guery, F. Hild, F. Latourte, S. Roux, International Journal of Plasticity, 81 (2016) 249-266.
[22] J. Hure, S. El Shawish, L. Cizelj, B. Tanguy, Journal of Nuclear Materials, 476 (2016) 231-242.
[23] D.-F. Li, N.P. O'Dowd, C.M. Davies, S.-Y. Zhang, European Journal of Mechanics - A/Solids, 30 (2011) 748-760.
[24] D.-F. Li, N.P. O'Dowd, Journal of the Mechanics and Physics of Solids, 59 (2011) 2421-2441.
[25] D. Gonzalez, J.F. Kelleher, J. Quinta da Fonseca, P.J. Withers, Materials Science and Engineering: A, 546 (2012) 263-271.
[26] B. Chen, J.N. Hu, P.E.J. Flewitt, D.J. Smith, A.C.F. Cocks, S.Y. Zhang, Acta Materialia, 67 (2014) 207-219.
[27] B. Chen, J.N. Hu, Y.Q. Wang, S.Y. Zhang, S. Van Petegem, A.C.F. Cocks, D.J. Smith, P.E.J. Flewitt, Acta Materialia, 85 (2015) 229-242.
[28] S. Hasunuma, T. Ogawa, International Journal of Fatigue, 127 (2019) 488-499.

[29] M.P. Petkov, J. Hu, E. Tarleton, A.C.F. Cocks, International Journal of Solids and Structures, 171 (2019) 54-80.
[30] T.O. Erinosho, K.A. Venkata, M. Mostafavi, D.M. Knowles, C.E. Truman, International Journal of Solids and Structures, 139-140 (2018) 129-137.
[31] Y.Q. Wang, M.W. Spindler, C.E. Truman, D.J. Smith, Materials & Design, 95 (2016) 656-668.
[32] Y.Q. Wang, H.E. Coules, C.E. Truman, D.J. Smith, International Journal of Solids and Structures, 135 (2018) 219-232.
[33] Y.Q. Wang, S. Hossain, S. Kabra, S.Y. Zhang, D.J. Smith, C.E. Truman, Journal of Materials Science, 52 (2017) 7929-7936.
[34] G.I. Taylor, Journal of the Institute of Metals, 62 (1938) 307-324.
[35] R. Hill, Journal of the Mechanics and Physics of Solids, 14 (1966) 95-102.
[36] J.R. Rice, Journal of the Mechanics and Physics of Solids, 19 (1971) 433-455.
[37] R. Hill, J.R. Rice, Journal of the Mechanics and Physics of Solids, 20 (1972) 401-413.
[38] S. Sadik, A. Yavari, Mathematics and Mechanics of Solids, (2015).
[39] Y. Huang, in, Division of Applied Sciences, Harvard University, Cambridge, Massachusetts, 1991.
[40] B. Xu, Y. Jiang, International Journal of Plasticity, 20 (2004) 2161-2178.
[41] W. Hutchinson John, R. Hill, Proceedings of the Royal Society of London. A. Mathematical and Physical Sciences, 348 (1976) 101-127.
[42] R.J. Asaro, A. Needleman, Acta Metallurgica, 33 (1985) 923-953.
[43] M. Ghorbani Moghaddam, A. Achuthan, B.A. Bednarcyk, S.M. Arnold, E.J. Pineda, Materials Science and Engineering: A, 703 (2017) 521-532.
[44] R.D. McGinty, D.L. McDowell, Journal of engineering materials and technology, 126 (2004) 285-291.
[45] B.S. Fromm, K. Chang, D.L. McDowell, L.Q. Chen, H. Garmestani, Acta Materialia, 60 (2012) 5984-5999.
[46] J. Hu, B. Chen, D.J. Smith, P.E.J. Flewitt, A.C.F. Cocks, International Journal of Plasticity, 84 (2016) 203-223.
[47] P.J. Armstrong, C.O. Frederick, in: G.E.G.B. Report RD/B/N, Central Electricity Generating Board, 1966.
[48] B.D. Smith, D.S. Shih, D.L. McDowell, International Journal of Plasticity, 101 (2018) 1-23.
[49] A.S. Khan, P. Cheng, International Journal of Plasticity, 12 (1996) 147-162.
[50] R.D. McGinty, D.L. McDowell, Journal of Engineering Materials and Technology, 121 (1999) 203-209.
[51] M.F. Horstemeyer, D.L. McDowell, Mechanics of Materials, 27 (1998) 145-163.
[52] W.J. Duffin, F.A. Nichols, Journal of Nuclear Materials, 45 (1973) 302-316.
[53] A. Staroselsky, B.N. Cassenti, Mechanics of Materials, 42 (2010) 945-959.
[54] A. Staroselsky, B.N. Cassenti, International Journal of Solids and Structures, 48 (2011) 2060-2075.
[55] D. Leidermark, M. Segersäll, Computational Materials Science, 90 (2014) 61-70.
[56] F. Liu, A.C.F. Cocks, E. Tarleton, (In Review), (2019).
[57] R.W. Bailey, Journal of the Institute of Metals, 35 (1926) 27-40.
[58] E. Orowan, Journal of the West of Scotland Iron and Steel Institute, 54 (1946) 45-53.
[59] L. Shi, D.O. Northwood, Acta Metallurgica et Materialia, 42 (1994) 871-877.
[60] L.N. McCartney, The Philosophical Magazine: A Journal of Theoretical Experimental and Applied Physics, 33 (1976) 689-695.
[61] J.H. Gittus, The Philosophical Magazine: A Journal of Theoretical Experimental and Applied Physics, 23 (1971) 1281-1296.
[62] R.W. Evans, B. Wilshire, Introduction to Creep, The Institute of Materials, London, 1993.
[63] A.A. Mamun, C. Simpson, T. Erinosho, D. Agius, C. Reinhard, M. Mostafavi, D. Knowles, in: ASME 2019 Pressure Vessels & Piping Conference, San Antonio, TX, USA, 2019.
[64] J. Harder, International Journal of Plasticity, 15 (1999) 605-624.

[65] H. Conrad, J. Narayan, Scripta materialia, 11 (2000) 1025-1030.
[66] H.H. Fu, D.J. Benson, M.A. Meyers, Acta Materialia, 49 (2001) 2567-2582.
[67] DREAM3D, in, http://dream3d.bluequartz.net/, 2018.
[68] DassaultSystèmes, in, 2018.
[69] R.K. Verma, P. Biswas, Materials Science and Technology (United Kingdom), 32 (2016) 1553-1558.
[70] R. Voothaluru, C.R. Liu, Fatigue and Fracture of Engineering Materials and Structures, 37 (2014) 671-681.
[71] M. Naderi, M. Amiri, N. Iyyer, P. Kang, N. Phan, Fatigue & Fracture of Engineering Materials & Structures, 39 (2015) 167-179.
[72] Z. Zhang, M.A. Cuddihy, F.P.E. Dunne, Proceedings of the Royal Society A: Mathematical, Physical and Engineering Sciences, 471 (2015).
[73] R.J. Kashinga, L.G. Zhao, V.V. Silberschmidt, F. Farukh, N.C. Barnard, M.T. Whittaker, D. Proprentner, B. Shollock, G. McColvin, Materials Science and Engineering: A, 708 (2017) 503-513.
[74] A.H. Cottrell, Dislocations and plastic flow in crystals, Clarendon, Oxford, England, 1953.
[75] F.J. Harewood, P.E. McHugh, Computational Materials Science, 39 (2007) 481-494.
[76] L. Kloc, V. Skienička, J. Ventruba, Materials Science and Engineering: A, 319-321 (2001) 774-778.
[77] Y. Wang, C.E. Truman, D.J. Smith, in: Structural Mechanics in Reactor Technology, Manchester, 2015.
[78] D. Peirce, C.F. Shih, A. Needleman, Computers & Structures, 18 (1984) 875-887.